batteries

MDPI

Article

Modeling and Simulation of a Gas-Exhaust Design for Battery Thermal Runaway Propagation in a $LiFePO_4$ Module

Songtong Zhang [1], Xiayu Zhu [1], Jingyi Qiu [1,*], Chengshan Xu [2], Yan Wang [3] and Xuning Feng [2]

[1] Chemical Defense Institute, Beijing 100191, China; songtong198999@163.com (S.Z.); zhuxy89@126.com (X.Z.)
[2] School of Vehicle and Mobility, Tsinghua University, Beijing 100084, China; xcs_pcg@mail.tsinghua.edu.cn (C.X.); fxn17@tsinghua.edu.cn (X.F.)
[3] College of Mechanical and Automotive Engineering, Qingdao University of Technology, Qingdao 266520, China; wangyan2387@163.com
* Correspondence: qiujingyi1202@163.com

Abstract: The release of flammable gases during battery thermal runaway poses a risk of combustion and explosion, endangering personnel safety. The convective and diffusive properties of the gas make it challenging to accurately measure gas state, complicating the assessment of the battery pack exhaust design. In this paper, a thermal resistance network model is established, which is used to calculate the battery thermal runaway propagation. Gas accumulation after thermal runaway venting of a $LiFeO_4$ module is studied using ANSYS Fluent under different venting schemes. The results show that the scheme of battery inversion and simultaneous exhaust from the side and bottom of the module is optimal. The methods and results presented can guide the design of $LiFeO_4$ cell pack runners.

Keywords: thermal runaway; thermal runaway propagation; venting gas; runner design

Citation: Zhang, S.; Zhu, X.; Qiu, J.; Xu, C.; Wang, Y.; Feng, X. Modeling and Simulation of a Gas-Exhaust Design for Battery Thermal Runaway Propagation in a $LiFePO_4$ Module. *Batteries* **2024**, *10*, 176. https://doi.org/10.3390/batteries10060176

Academic Editor: Vilayanur Viswanathan

Received: 25 March 2024
Revised: 4 May 2024
Accepted: 14 May 2024
Published: 24 May 2024

1. Introduction

Energy is the source of social operation [1–3]. Lithium-ion batteries are commonly used as electric energy carriers, diversifying the energy structure. Lithium-ion batteries have been widely used in automobiles and energy storage stations because of their high energy density [4], reusability and decreasing production costs. Lithium-ion batteries suffer from thermal runaway (TR) under mechanical [5], thermal [6] and electrical abuse [7,8]. Battery thermal runaway has become a household name, which makes consumers worried when buying electric vehicles [9].

The main hazards of TR are high temperature [10,11] and venting combustion gas [12–14]. In battery packs, the TR of one cell will induce thermal runaway propagation (TRP) [15–17], which seriously threatens the life safety of the passenger. In electric vehicle safety accidents, heat abuse is the main cause of the TRP [15]. Jin et al. [6,18] studied the influence of different heating power rates on the thermal runaway of the battery. It has been shown that the thermal propagation time with a heating power of 200 W is less than 2000 W. The preheating effect accelerates the TRP. Different heating positions of $LiFePO_4$(LFP) batteries also affect TR behavior [19]. Thermal runaway caused by heat on the large wall of the cell takes less time than heat on the bottom and sides of the cell. In addition, the TR venting gas-flow velocity of heating from large wall is fastest, followed by bottom surface and side surface. Jia et al. [20] compared the effects of different pre-loading forces on thermal runaway of LFP cells. A higher cell pre-load would result in a higher jet velocity in the TR. In addition, the amount of gas produced by the eruption would be higher. Heat pads are often used in battery modules to block the TRP. The TRP behavior can be delayed or even blocked by the low thermal conductivity of the heat pad. As an important part of the battery thermal management, the liquid cooling plate can also ease the TRP time, giving passengers more time to escape. Zhang et al. [21] combined heat

insulation pad with liquid cooling and transferred heat to the liquid cooling plate through the heat insulation pad, so that the TR energy of the battery is taken away by the liquid cooling plate to delay the TRP time.

LFP cells have excellent thermal safety properties. Compared with $LiNi_xCo_yMnzO_2$ (NCM) batteries, the maximum temperature of TR is lower, and the temperature rise rate is smaller [22]. However, the combustible gas from safety valve of the LFP battery slowly accumulates in the battery pack, bringing a potential explosion risk [23–25]. This phenomenon may be more dangerous than the TR of NCM cells. Wang et al [24] found that the explosion overpressure of LFP cell gas was twice that of NCM cells in the thermal runaway gas test of batteries with different systems. This further illustrates the need for gas safety protection of LFP batteries. Venting gas is a non-negligible role in TR [26–29]. High concentration of gas venting from battery packs can easily cause combustion, thus burning the entire vehicle body [30]. The burning flame of the car also further accelerate the battery pack TRP, creating a vicious circle. The CFD method can be used to predict the flammable gas flow during TRP. Existing TR and TRP models typically calculate the entire 3D temperature field of the battery. However, in the design of gas channels, calculating the 3D temperature field of the battery is redundant. Therefore, it is necessary to reduce the dimensionality of the existing thermal runaway heat transfer model.

The convective diffusion properties of combustible gases and the stochastic nature of the TR eruption test hinder the design of battery gas safety protection. Gas channels are an important component of TR outgassing. In this paper, numerical studies of gas-flow channels are carried out. Based on the flow path design, an external intake is added, and the influence of external intake and different flow paths on TR exhaust is analyzed, which can bring enlightenment to the design of battery pack gas-flow path.

2. Battery Thermal Runaway Propagation Model

Heat generation is the main feature of thermal runaway. The heat conduction inside the cell and the thermal reaction of the material is intensified with the increase in temperature. Battery jelly roll and internal air can be considered a solid, and the energy conservation equation in solid zone reads [31]:

$$\rho C_p \frac{dT}{dt} = Q_{gen} \tag{1}$$

The thermal reaction of the cell material intensifies as the temperature increases. The materials reaction include decomposition of the solid electrolyte interphase (SEI) layer, reaction between anode and electrolyte, decomposition of the SEI layer, reaction between anode and electrolyte, separator melting and internal short circuit, reaction between cathode and electrolyte, decomposition of electrolyte and Binder reaction. The thermal runaway heat-generation source item can be simplified by [26]:

$$Q_{gen} = \frac{1}{V} H \frac{dc_b}{dt} \tag{2}$$

$$\frac{dc_b}{dt} = \begin{cases} \frac{\rho_b V_b C_{p,bat}}{\Delta H_b} \left(\frac{dT}{dt}\right)_{ARC} & (T_1 < T_{bat} < T_2, 0 \le c \le 1) \\ c_1 & (T_{bat} \ge T_2, 0 \le c \le 1) \\ 0 & (else) \end{cases} \tag{3}$$

Thermal runaway batteries heat up rapidly, creating a temperature difference. Heat is transferred by thermal conduction to the cell without thermal runaway:

$$Q_{con} = \lambda A \frac{dT}{dx} \tag{4}$$

There is a convection of heat between the cell and a fluid medium, such as air. The equation of heat convection between cell and fluid can be written as:

$$Q_{cov} = hA\Delta T \tag{5}$$

In addition, radiative heat dissipation is a non-negligible item in thermal runaway:

$$Q_{rad} = \varepsilon A\sigma(T_1^4 - T_2^4) \tag{6}$$

Equations (1)–(6) are sufficient to build a thermal runaway heat-generation model. The simplest method for thermal runaway venting behavior is to obtain eruption boundary conditions experimentally. The boundary conditions are then assigned to the TR model. Therefore, the acquisition of the eruption boundary conditions is introduced in the experiment.

The thermal reaction of the cell material creates gases and accumulates inside. When the safety valve threshold is reached, the gas is expelled from the cell. The emitted gases include H_2, C_2H_4, CH_4, CO_2, CO, etc. The continuity and momentum equations of multi-component gas flow are listed as follows [32]:

$$\frac{\partial \rho}{\partial t} + \nabla \cdot (\rho \vec{v}) = S_m \tag{7}$$

$$\frac{\partial}{\partial t}(\rho \vec{v}) + \nabla \cdot (\rho \vec{v}\vec{v}) = -\nabla p + \nabla \cdot (\bar{\bar{\tau}}) + \rho \vec{g} + \vec{F} \tag{8}$$

Multi-component gas-flow heat transfer needs to consider the energy transfer caused by different gas diffusion coefficients, and its energy equation is as follows:

$$\frac{\partial}{\partial t}(\rho E) + \nabla \cdot (\vec{v}(\rho E + p)) = -\nabla \cdot (k_{eff}\nabla T - \sum_j h_j \vec{J_j}) + S_h \tag{9}$$

In addition, calculating the spatial distribution of each component in a multi-component gas requires solving the mass fraction equation:

$$\frac{\partial}{\partial t}(\rho Y_i) + \nabla \cdot (\rho \vec{v} Y_i) = -\nabla (pD_{i,m} + \frac{\mu_t}{Sc_t})\nabla Y_i + R_i + S_i \tag{10}$$

The standard $k-\varepsilon$ turbulence model is considered with the standard wall function as follows [21]:

$$\begin{aligned} \tfrac{\partial}{\partial t}(\rho k) + \tfrac{\partial}{\partial x_i}(\rho k u_i) = \tfrac{\partial}{\partial x_j}[(\mu + \tfrac{\mu_t}{\sigma_k})\tfrac{\partial k}{\partial x_j}] + G_k \\ + G_b - \rho\varepsilon - Y_M + S_k \end{aligned} \tag{11}$$

$$\begin{aligned} \tfrac{\partial}{\partial t}(\rho \varepsilon) + \tfrac{\partial}{\partial x_i}(\rho \varepsilon u_i) = \tfrac{\partial}{\partial x_j}[(\mu + \tfrac{\mu_t}{\sigma_k})\tfrac{\partial \varepsilon}{\partial x_j}] + \\ C_{1\varepsilon}\tfrac{\varepsilon}{k}(G_k + G_{3\varepsilon}G_b) - G_{2\varepsilon}\rho\tfrac{\varepsilon^2}{k} + S_\varepsilon \end{aligned} \tag{12}$$

Based on the above theory, thermal resistance network models of 3 batteries and 16 batteries were established by MATLAB R2022a, which calculates the temperature and time of TR. The basic parameters of the model are shown in Table 1. The experimental venting results are assigned to the nozzle of the cell safety valve. The 3D gas venting model was established by ANSYS Fluent 2023R1.

Figure 1 shows the boundary conditions of the TRP. The boundary conditions include conductive heat transfer, convective heat transfer, thermal resistance and radiative heat transfer. The battery thermal runaway is triggered by external heating, with a heating power of 400 W. The heating is stopped when the cell temperature is greater than 750 K.

Figure 2 shows the geometry and mesh of the LFP cell module. The cell module has 16 cells. The mesh is generated by Fluent meshing with a mesh number of 210,056. The mesh contains 16 cells and an air zone at the top of the cell module. The safety valves are

defined as inlets, and there are 16 of them in total. In addition, nine walls/inlets are split at the top of the aerial zone. Two outlets/inlets are defined on the side of the air zone to drain the TR gas. The calculated cases are summarized in Table 2.

Table 1. Thermal resistance network model parameters.

Cell and air	Conductive heat transfer	area = 0.00767 m^2; thickness = 0.001 m; λ = 500 W $m^{-1}K^{-1}$
	Convective heat transfer	area = 0.007678 m^2; h = 5 W $m^{-2}K^{-1}$
	Radiative heat transfer	area = 0.007678 m^2; ε = 0.04 W $m^{-2}K^{-4}$
Cell front face	Conductive heat transfer	area = 0.00923 m^2; thickness = 5.8 mm; λ = 0.29 W $m^{-1}K^{-1}$
Cell side face	Conductive heat transfer	area = 0.00143 m^2; thickness = 5.8 mm; λ = 0.29 W $m^{-1}K^{-1}$
Heater to cell	Conductive heat transfer	area = 0.00923 m^2; thickness = 5.8 mm; λ = 0.29 W $m^{-1}K^{-1}$
ρ	Density	2132.86 kg m^{-3}
c_p	Specific heat	1089.35 J kg^{-1} K^{-1}
m	Mass	433.10 g
V	Volume	142 mm × 65 mm × 22 mm
ε	Emissivity	0.58
σ	Boltzmann constant	5.67 × 10^{-8} W m^{-2} K^{-4}
T_1	Self-generated heat temperature	166.92 °C
T_2	TR onset temperature	274.00 °C
T_3	TR maximum temperature	607.00 °C
H	TR total energy	207,628.64 J

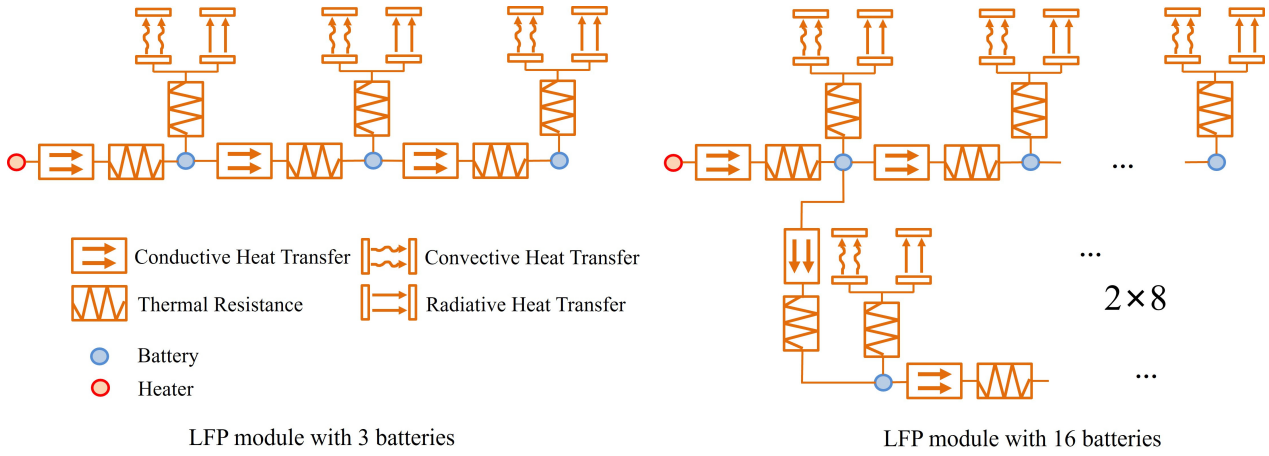

Figure 1. Boundary conditions of battery thermal runaway propagation.

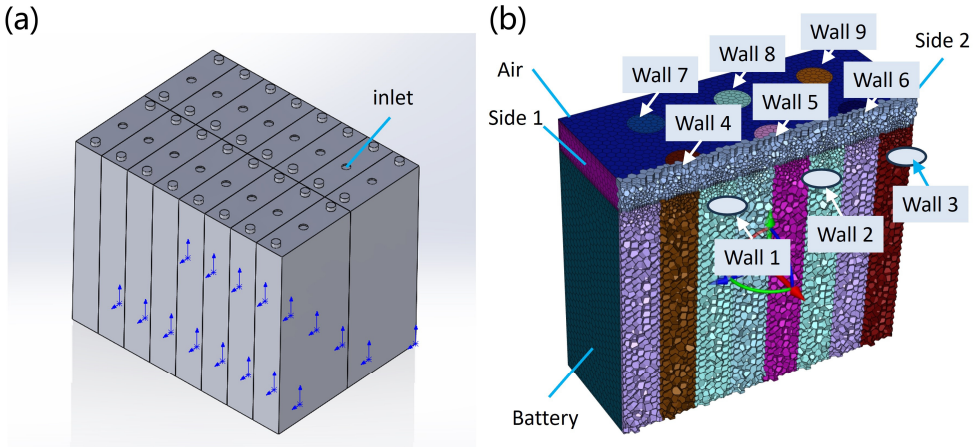

Figure 2. LFP battery module geometry and mesh. (**a**) The module consists of 16 LFP cells. (**b**) Battery module mesh is generated by Fluent meshing.

Table 2. Flow path calculation summary.

Case	State	Side 1	Side 2	Wall 1	Wall 2	Wall 3	Wall 4	Wall 5	Wall 6	Wall 7	Wall 8	Wall 9
Case 1	Upright	Outlet	Outlet	Wall	Wall	Wall	Wall	Wall	Wall	Wall	Wall	Wall
Case 2	Upright	Outlet	Outlet	Wall	Wall	Wall	Wall	Inlet 1.5 g/s	Wall	Wall	Wall	Wall
Case 3	Upright	Outlet	Outlet	Wall	Wall	Wall	Inlet 1.5 g/s	Wall	Wall	Wall	Wall	Wall
Case 4	Upright	Outlet	Outlet	Inlet 1.5 g/s	Wall	Wall	Wall	Wall	Wall	Wall	Wall	Wall
Case 5	Upright	Outlet	Outlet	Wall	Wall	Wall	Wall	Inlet 1.0 g/s	Wall	Wall	Wall	Wall
Case 6	Upright	Outlet	Outlet	Wall	Wall	Wall	Wall	Inlet 2.0 g/s	Wall	Wall	Wall	Wall
Case 7	Upright	Outlet	Outlet	Wall	Wall	Wall	Wall	Inlet 2.5 g/s	Wall	Wall	Wall	Wall
Case 8	Upright	Inlet 1.0 g/s	Outlet	Wall	Wall	Wall	Wall	Wall	Wall	Wall	Wall	Wall
Case 9	Upright	Inlet 1.5 g/s	Outlet	Wall	Wall	Wall	Wall	Wall	Wall	Wall	Wall	Wall
Case 10	Upright	Inlet 2.0 g/s	Outlet	Wall	Wall	Wall	Wall	Wall	Wall	Wall	Wall	Wall
Case 10	Upright	Inlet 2.5 g/s	Outlet	Wall	Wall	Wall	Wall	Wall	Wall	Wall	Wall	Wall
Case 12	Invert	Outlet	Outlet	Wall	Wall	Wall	Wall	Wall	Wall	Wall	Wall	Wall
Case 13	Invert	Outlet	Outlet	Outlet	Outlet	Outlet	Outlet	Outlet	Outlet	Outlet	Outlet	Outlet
Case 14	Invert	Inlet 1.0 g/s	Outlet	Outlet	Outlet	Outlet	Outlet	Outlet	Outlet	Outlet	Outlet	Outlet

3. Thermal Runaway Experiment

In this paper, the TRP venting model is established. The Accelerating Rate Calorimeter (ARC) test and the TRP test of cell module are carried out. The ARC test can obtain the characteristic temperature of the TR and the self-generated heat process of the cell. ARC tests can be used to model cell heat generation. The test involved implanting a thermocouple inside the cell and repairing the location of the breach.

The ARC operates in a heat–wait–seek mode. Prior to initiating this mode, the ARC continuously heats the battery until its temperature reaches 25 °C. After that, it enters the heat–wait–seek mode. The temperature ramp for heating is set at 5 °C. Once the ARC temperature exceeds the battery temperature by 5 °C, it enters the wait and seek state. During this state, it waits for the battery temperature to gradually align with the ARC temperature and monitors whether the temperature rise of the battery reaches 0.02 °C/min. If the condition is met, the ARC proceeds to the exotherm mode. In the exotherm mode, the temperature of the ARC is consistent with the temperature of the cell, which avoids the dissipation of heat from the cell. If the battery's temperature rise does not meet the self-heating criteria, once the battery temperature aligns with the ARC, the ARC continues to increase by 5 °C and re-enter the wait–seek mode.

Figure 3 shows the internal central temperature and the temperature rise rate of the cell. The temperature is measured by a built-in thermocouple in the cell. The initial thermal runaway temperature of the cell is 166.92 °C. The thermal runaway temperature of the cell is 274.00 °C. The maximum temperature of the cell is 607 °C.

Figure 4 shows the TRP experiment with three cells. TR is triggered by side heating and the battery is in 100% SOC state. The TR results of different TR triggering methods are different. In battery safety accidents, the TRP mode is mainly caused by heat transfer from the cell surface. Therefore, the side heating is chosen to trigger the TR. The heating surface is the large wall of the cell with a heating power of 400 W. The thermocouple is attached to the battery surface using polyimide tape. The attachment position is shown in Figure 4a. Figure 4b shows the cell module structure and thermocouple location. The thermocouple

is set in the center of the front and back face of the cell. Figure 4c,d shows the venting behavior of LFP cell. The first venting of the smoke, after the safety valve was opened, maintained 73 s. The second venting lasted 60 s. According to the literature [24], the gas released by the first eruption of this LFP cell is 8.8 L, and the gas released by the second venting is 6.61 L. Using 30.6 L/mol as a criterion, the first released gas is 0.2876 mol and the second released gas is 0.2224 mol. The molar mass of the venting gas is 1.1488 g/mol. The average mass flow rate of gas in the initial 73 s is 0.0045 g/s. The average mass flow rate of gas in the second venting is 0.00426 g/s. The mass flow rate of the cell gas is obtained and assigned to the cell safety valve, for which a TR venting model has been developed.

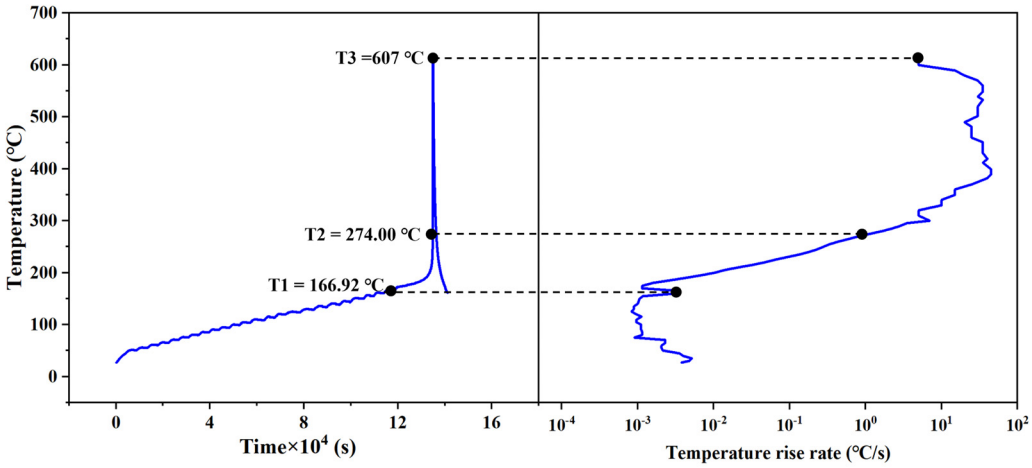

Figure 3. Internal center temperature and temperature rise rate of the battery.

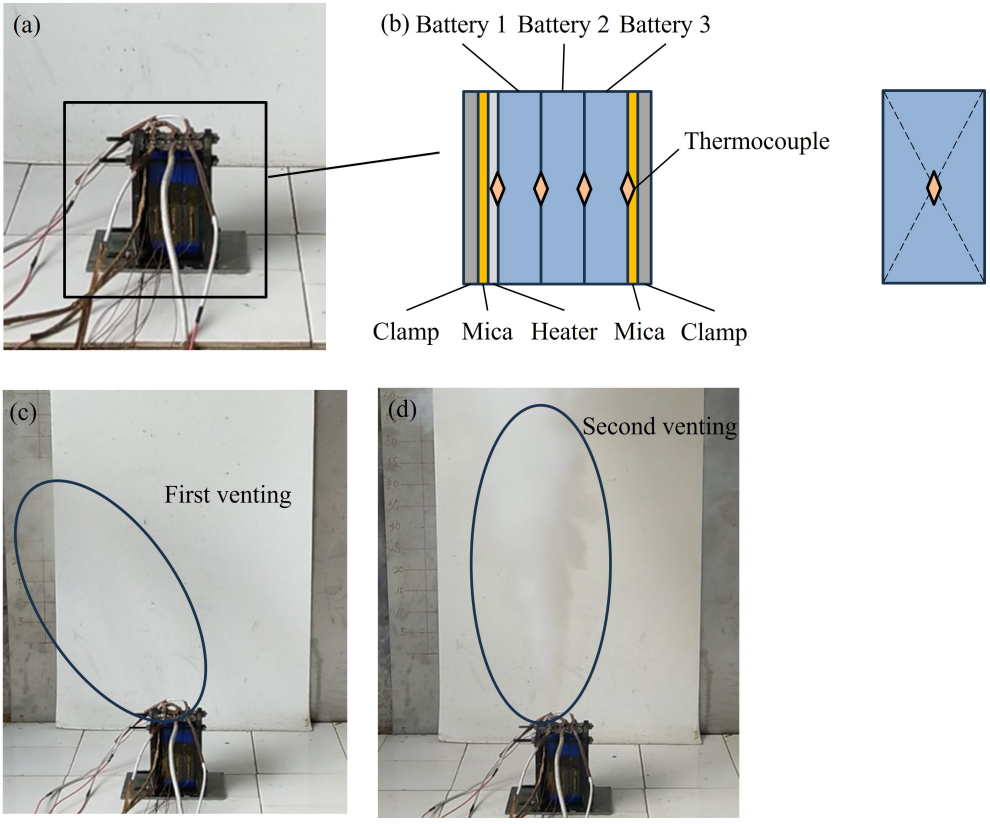

Figure 4. Battery thermal runaway propagation experiment, thermal runaway trigger mode is side heating. (**a**) Experimental scenarios and batteries. (**b**) Battery module structure and thermocouple location. (**c**) First venting of LFP battery thermal runaway. (**d**) second venting of LFP battery runaway.

4. Results and Discussion

Figure 5 presents a comparison of the experimental and simulation temperature results. The first battery in the experiment reached a peak temperature of 769 °C at 411 s, while the simulation model reached a peak temperature of 749 °C at 413 s. The second battery in the experiment reached a peak temperature of 739 °C at 701 s, and the simulated second battery reached a peak temperature of 752 °C at 708 s. The third battery in the experiment reached a peak temperature of 759 °C at 859 s, and the simulated third battery reached a peak temperature of 763 °C at 880 s. The details of the Lump model developed in this paper do not agree with the experimental results. However, key parameters of the TR, such as the TR time and the TR temperature, can be predicted. Figure 6 shows the TRP temperature and the sequence of 16 cell modules. The TR of the cell has propagation properties. The temperature of a TR cell is much higher than that of an adjacent cell. The heat is transferred to other cells, triggering their internal thermal decomposition reactions, resulting in TR. Finally, thermal runaway propagation occurs. Simulation results show that the TRP of 16 cells can be divided into three phases. Stage 1 is the first cell occurrence of TR. Stage 2 is when TR develops to the side of the cell in the module. Stage 3 involves synchronous thermal runaway propagation. In our study, the first TR event occurred at 424 s. The heat is transferred to neighboring cells. By 1000 s, a total of four batteries experienced TR. By 1000 s–2000 s, TR occurred in 12 batteries that were permanently repaired. The thermal runaway propagation time gradually increases, and the first column cell and the second column cell have synchronized TRP, which accelerates the TRP propagation.

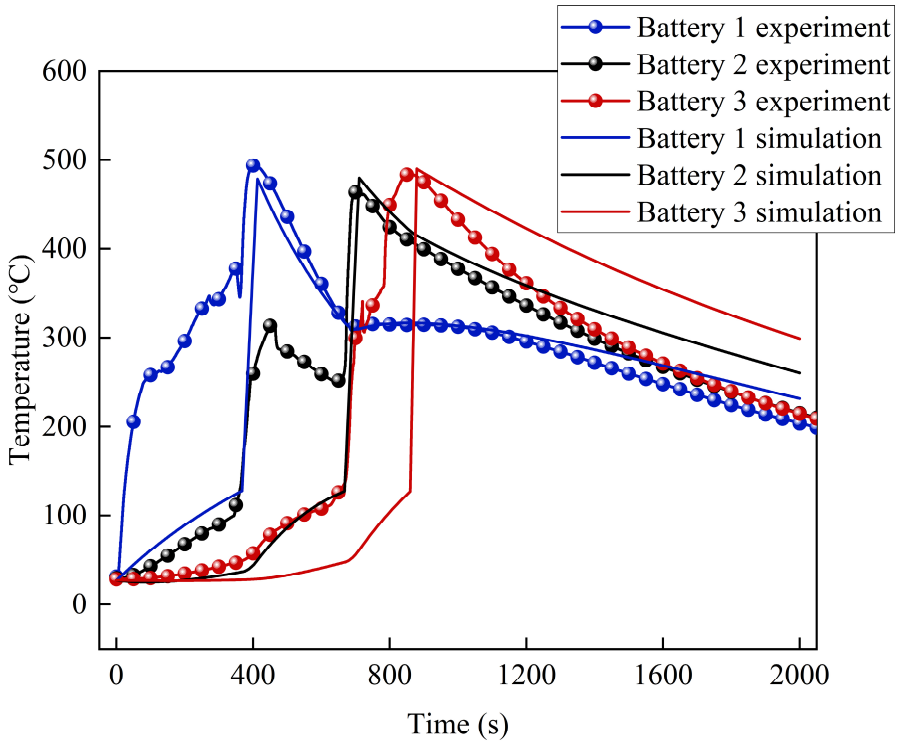

Figure 5. Comparison of experimental and simulation temperature results.

TR is accompanied by venting behavior. These venting flammable gases remain inside the battery pack, posing a potential risk of combustion. The external air intake blows away combustible gases that build up inside the battery pack, reducing the risk of combustion and explosion. Figure 7 shows the calculation cases of cell TR venting with external ventilation. In the absence of external air intake, the flammable gas ejected from the battery mainly relies on the momentum of the safety valve to produce flow. However, when there is external air intake, the flammable gas ejected from the battery is driven by both the momentum of the safety valve and the external air intake, which may increase

the flow velocity of the flammable gas. Therefore, we conducted simulations for different intake velocities. In Case 1, there is no external intake. The gas emitted by the cell escapes naturally from both sides of the outlet. Case 2 has an external intake, which is located in wall5. Wall5 is the mass flow boundary condition with a mass flow rate of 1.5 g/s. The external air intake may be sourced from the car air conditioner. The air conditioner is assumed to provide ventilation during the TR of the battery pack. The mass flow rate of the car air conditioner is about 2.5 g/s. This means that when TR occurs, the maximum air intake provided by the car to the battery pack is less than 2.5 g/s. Therefore, 1.5 g/s was chosen as the mass outflow rate of the ingested air. The air intakes in cases 3 and 4 are located at walls 4 and walls 1, respectively. For no external intake, Case 1, the gas vented by the cell will diffuse in a conical upward direction from the safety valve. When the air hits the top, a stagnation region forms. The gas flows sideways from the stagnation region, creating a wall-jet region. The gas then flows out of the battery pack. The air intake gas flow impacts the top of the cell and causes reflection to flow to the sides. External intake changes the direction of the venting flow. The gas is blown out of the cell pack.

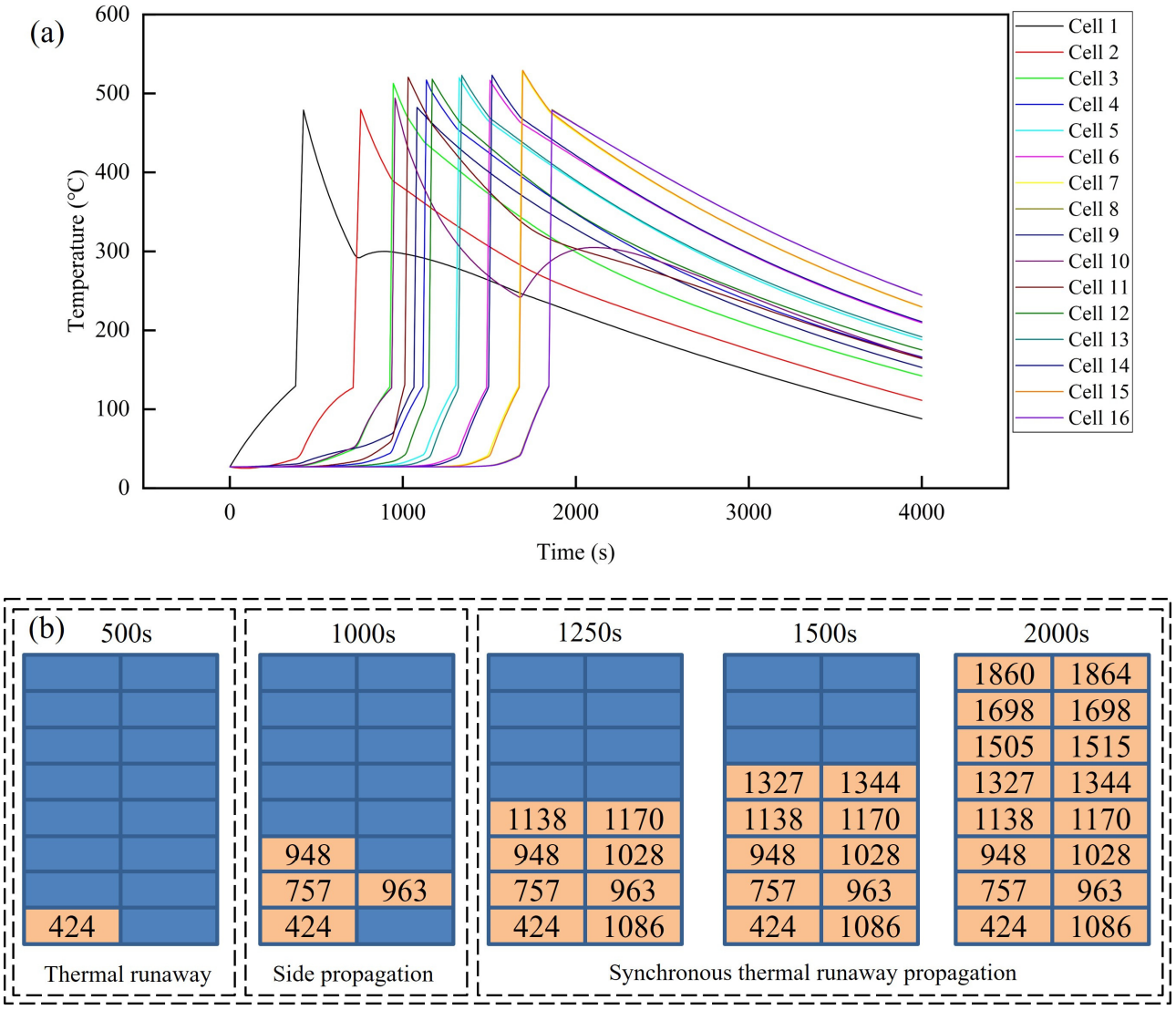

Figure 6. Thermal runaway propagation temperature and sequence of 16 battery modules. (**a**). Thermal runaway propagation temperature and onset time. (**b**) Time sequence of thermal runaway propagation.

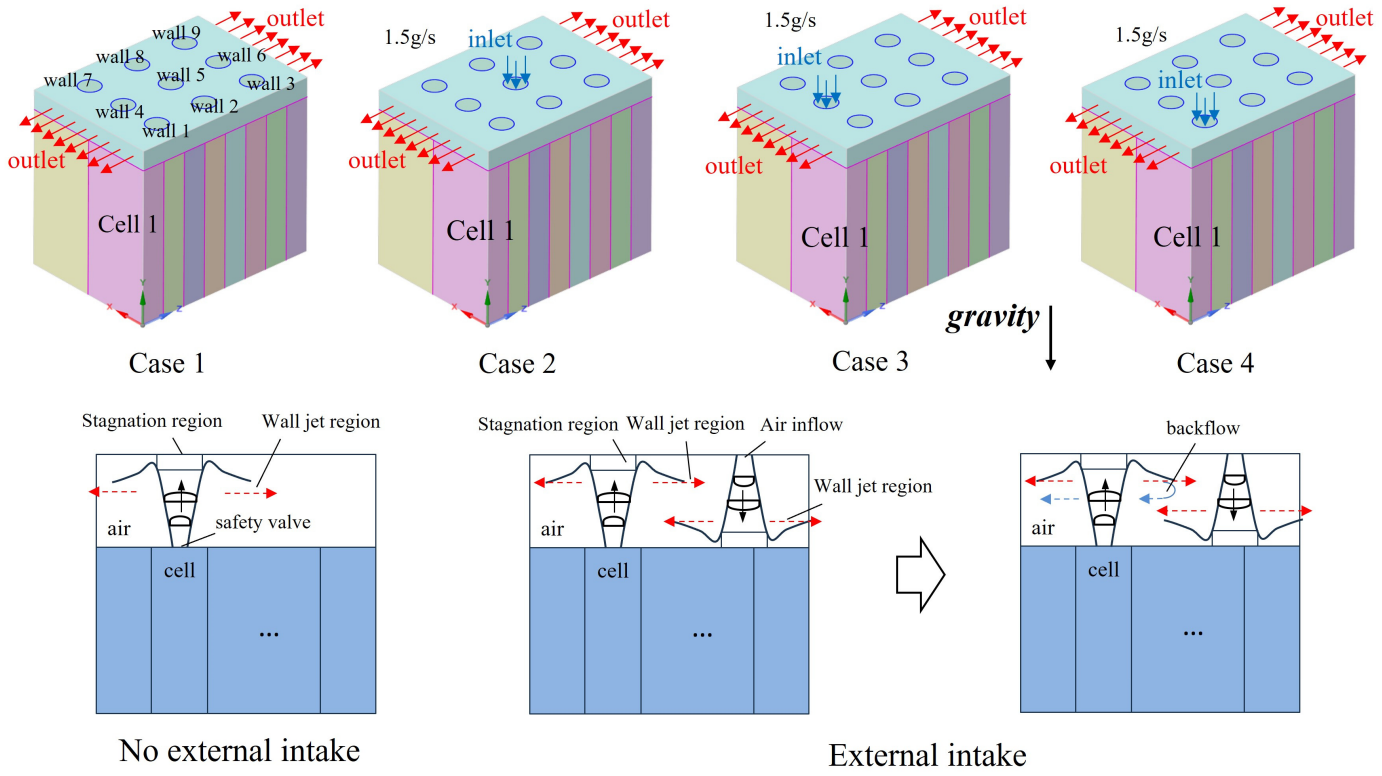

Figure 7. Influence of different ventilation positions on thermal runaway exhaust case 1 has no external intake. Case 2 has an external air intake located at wall5/inlet. Case 3 has an external intake, which is located at wall4/inlet. Case 4 has an external air intake located at wall1/inlet.

In the gas-flow calculation, the mass fraction equation needs to be solved for each gas flow. Gas components with small mass fractions need to be neglected to increase the speed of the calculation. In this paper, the gas flow of H_2, CH_4, C_2H_4, CO and CO_2 are considered. Figure 8 is volume average of mole fraction. The flow of different gas components is different due to the difference in gas fraction and diffusivity. In Figure 8a, CO_2 is a common component of air. Since backflow effects are taken into account in the computational model, the baselines for the CO_2 volume average mole fraction are different in different cases. Because of the small space of the calculated gas flow, there is no significant difference in the volume average of the mole fraction of gas for the different diffusion coefficients. The concentration of combustible gas immediately peaks when the cell is vented. The gas is driven away from the exit by the jet. External intake can accelerate the flow of combustible gas, which reduces the concentration of combustible gas during venting. Different intake positions can affect the venting results. Case 1 does not have an external air drive, so the concentration of combustible gases in the natural exhaust process is the highest. In Cases 2–4, there is no case in which the combustible gas fraction can always be kept at a minimum. This phenomenon is caused by a change in the position of the gas vent in the cell module. The TRP began to accelerate during the 1000 s–1800 s, and a large amount of combustible gas was vented. This resulted in a high concentration of combustible gases diffusing through the module. As a result, the risk of gas burning is highest during this period. Overall, Case 2 has the best venting effect. It is then necessary to discuss whether a higher mass outflow rate can further reduce the combustible gas concentration.

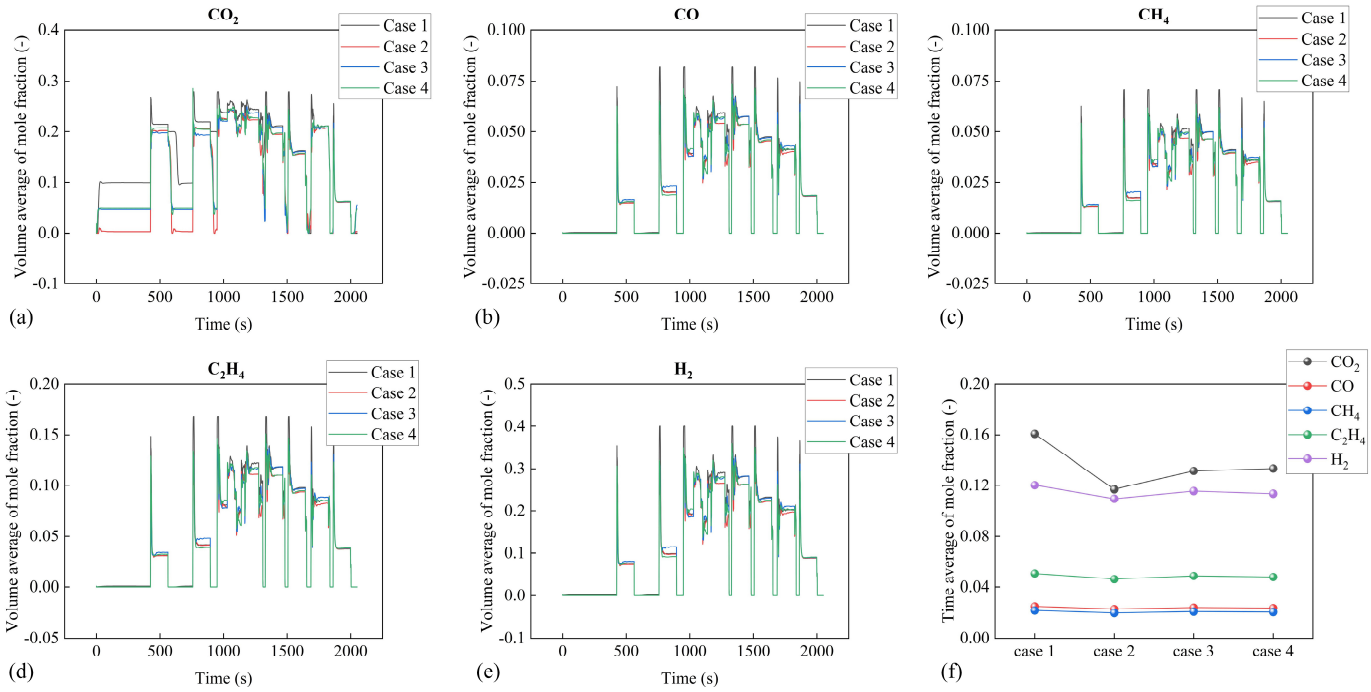

Figure 8. Volume average of mole fraction, which is obtained by Ansys Fluent. (**a**) Volume average of mole fraction of CO_2. (**b**) Volume average of mole fraction of CO. (**c**) Volume average of mole fraction of CH_4. (**d**) Volume average of mole fraction of C_2H_4. (**e**) Volume average of mole fraction of H_2. (**f**) Time average of mole fraction.

The effect of different intake mass outflow rates is discussed as shown in Figure 9. The inlet is also section wall5 based on Case 2. The TR gas concentration of the cell module under the mass flow rate of 1.0 g/s, 2.0 g/s and 2.5 g/s was calculated, respectively. The calculated results are displayed in Figure 10. Increasing the intake can reduce the concentration of combustible gas slightly in the battery pack. The results of the calculation show that the concentration of H2 drops by 2.4% when the mass flow rate of intake increases from 1.0 g/s to 1.5 g/s. When the intake mass flow rate increases from 1.5 g/s to 2.0 g/s, the H_2 concentration decreases by 3.2%. When the intake mass flow rate increases from 2.0 g/s to 2.5 g/s, the H_2 concentration decreases by 1.1%. Results indicate that a mass flow rate of 1.5 g/s can lead to improved cost efficiency, especially considering the limited air intake capacity in the car.

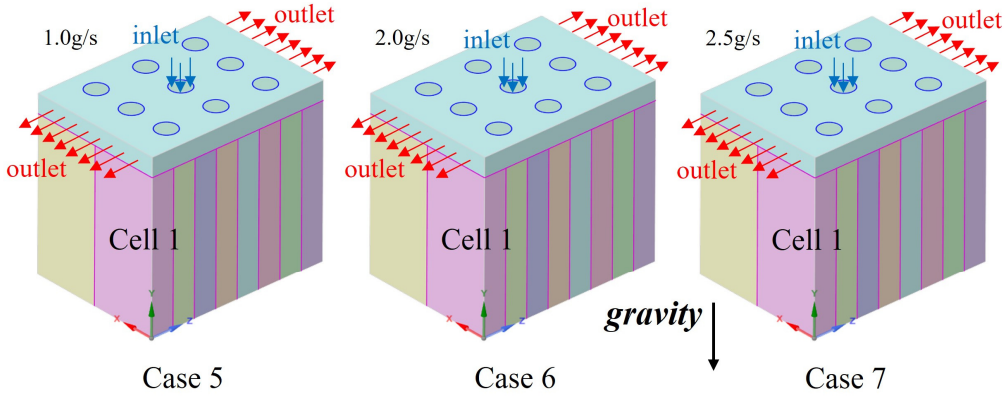

Figure 9. Different mass flow calculation Case diagram. Side of the module is outlet, and the wall5/inlet location is the inlet boundary condition. In Case 5, the mass flow is 1.0 g/s. In Case 6, the mass flow is 2.0 g/s. In Case 7, the mass flow is 2.5 g/s.

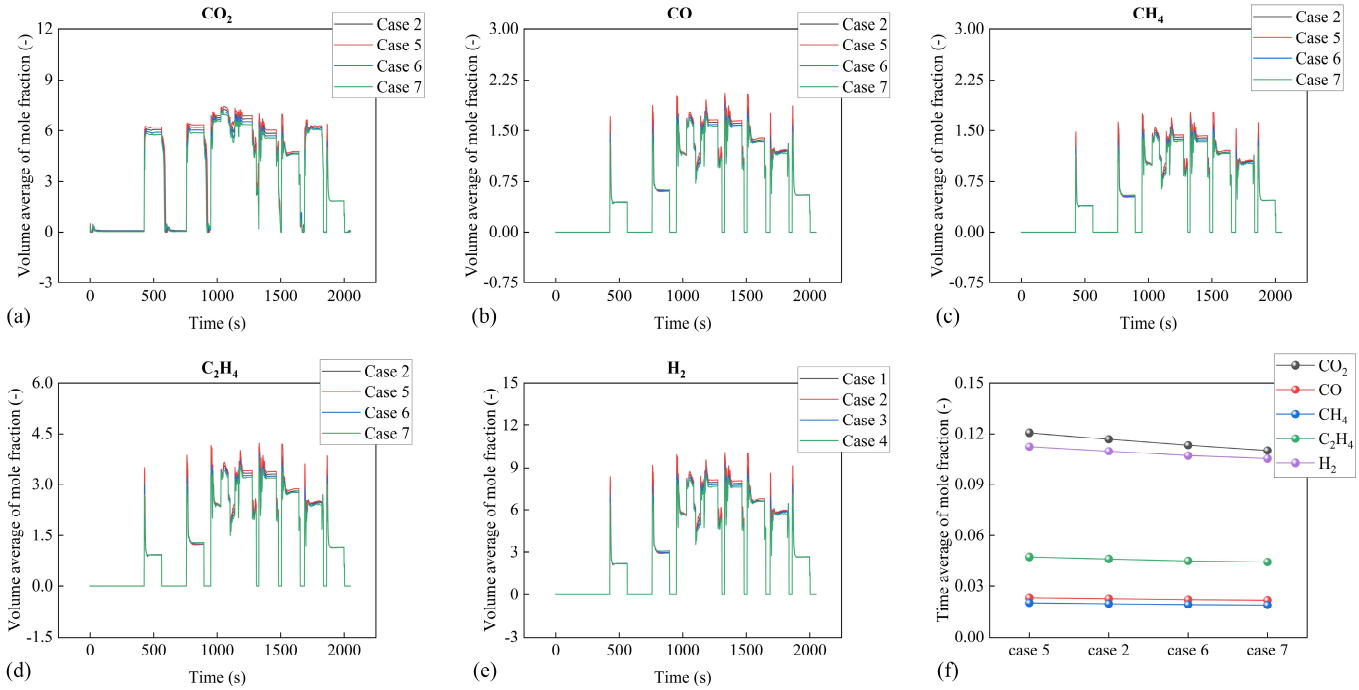

Figure 10. Influence of different inlet mass flow on gas concentration. The mass flow including 1.0 g/s, 1.5 g/s, 2.0 g/s and 2.5 g/s. (**a**) Volume average of mole fraction of CO_2. (**b**) Volume average of mole fraction of CO. (**c**) Volume average of mole fraction of CH_4. (**d**) Volume average of mole fraction of C_2H_4. (**e**) Volume average of mole fraction of H_2. (**f**) Time average of mole fraction.

The sides of the module can be used as air intakes. As shown in Figure 11, one side of the module acts as an inlet and the other side acts as an outlet. The top air intakes are all boundary conditions of the wall. The direction of gravity is towards the bottom of the cell. The mass flow rate of Case 8–11 intake air is 1.0 g/s, 1.5 g/s, 2.0 g/s and 2.5 g/s, respectively. Figure 12 shows the calculation results. In Case 8–11, side intake smooths the concentration of combustible gas. There is no significant peek in venting. The concentration of combustible gas in the cell module remains stable even when TRP occurs. This means that the stability of air intake and venting from the side is better than intake from the top. Since there is no significant peak, air intake from the side favors a safe design. As the peak is near the average, the safety design redundancy can be reduced. Moreover, increasing the mass flow can further decrease the concentration of combustible gas.

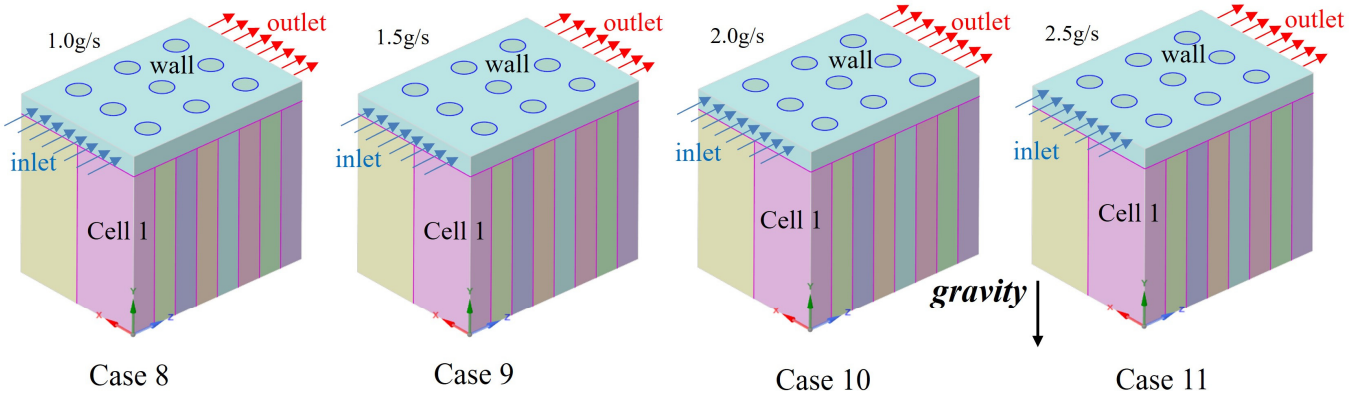

Figure 11. Different mass flow calculation Case diagram. Case 8 mass flow rate is 1.0 g/s. Case 9 mass flow rate is 1.5 g/s. Case 10 mass flow rate is 2.0 g/s. Case 11 mass flow rate is 2.5 g/s.

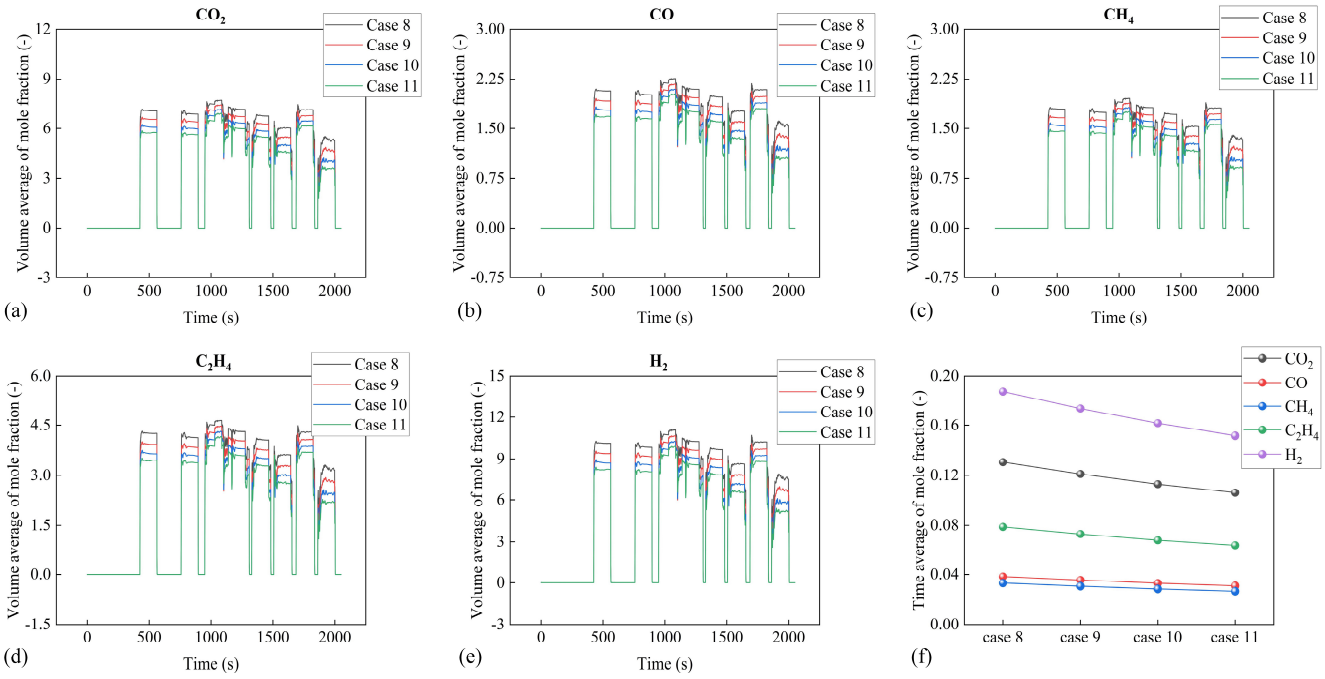

Figure 12. Different lateral intake mass flow. No outlet at the top. The mass flow including 1.0 g/s, 1.5 g/s, 2.0 g/s and 2.5 g/s. (**a**) Volume average of mole fraction of CO_2. (**b**) Volume average of mole fraction of CO. (**c**) Volume average of mole fraction of CH_4. (**d**) Volume average of mole fraction of C_2H_4. (**e**) Volume average of mole fraction of H_2. (**f**) Time average of mole fraction.

Flammable gases from the TR vent have a well-known risk of combustion. Continuous jet impacts and flames inside the battery pack may cause the top cap of the battery pack to melt. This would seriously endanger the life of the occupants. To avoid jets entering the cab, car companies have begun using battery design schemes with the safety valve facing down. Figure 13 shows the three exhaust methods with the cell safety valve facing down. The cell is inverted in Case 12. The boundary conditions on both sides of the module are outlet. The nine circular boundary conditions are all walls. Case 13 modifies nine circular boundary conditions to outlets based on Case 12. This allows the jet to be discharged directly from the bottom of the cell pack without passing through the flue on either side. Case 14 is based on Case 13 by adding air intake on one side of the module with an intake mass flow rate of 1.0 g/s. Figure 14 shows the calculation results. Case 12 has the weakest exhaust. It is conjectured that the exhaust area in Case 12 is smaller than that in Cases 12–14. Compared to Cases 13 and 14, the external intake does not improve the exhaust. The distance from the cell safety valve to the wall/outlet is smaller than the side outlet. The side intake interferes with the gas venting from the bottom wall/outlet. The best exhaust effect is in Case 13. In addition, Case 12 is compared with Case 1. The cell inversion did not significantly improve the exhaust effect.

Figure 15 shows the results of the calculations for all the exhaust schemes. The average concentration of H2 in top intake (Case 5–7) and side intake (Case 8–11) is around 0.12 and 0.16, respectively. The calculations show that the exhaust of the top intake is better than that of the side intake. Increasing the exhaust area improves the exhaust. The best exhaust is Case 13 among all the exhaust schemes. In Case 13, the cell is inverted, and the exhaust port contains both side and bottom exhausts. The time-averaged mole fraction can be reduced by 42.69% compared to Case 1. Case 13 has the best exhaust among all the calculated cases. The effect of the gas exhaust can be improved as the area of the exhaust increases.

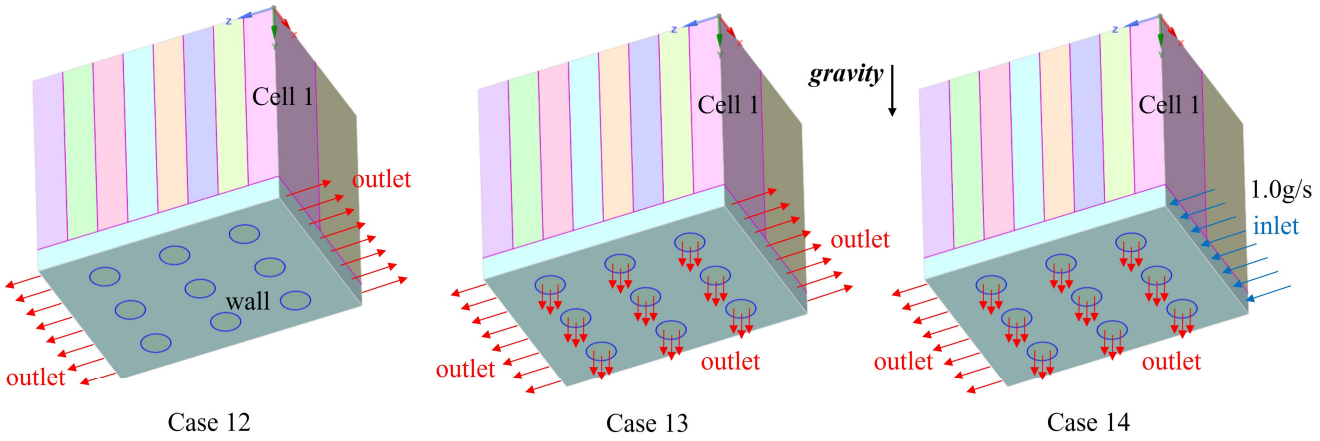

Figure 13. Battery upside down, safety valve facing the ground. Case 12 battery upside down. The boundary conditions on both sides of the module are outlet. Nine circular boundary conditions are wall. Case 13 Battery upside down. The boundary conditions on both sides of the module are outlet. Nine circular boundary conditions are outlets. Case 14 battery upside down. The boundary condition on one side of the module is inlet. The other side is an outlet. Nine circular boundary conditions are outlets.

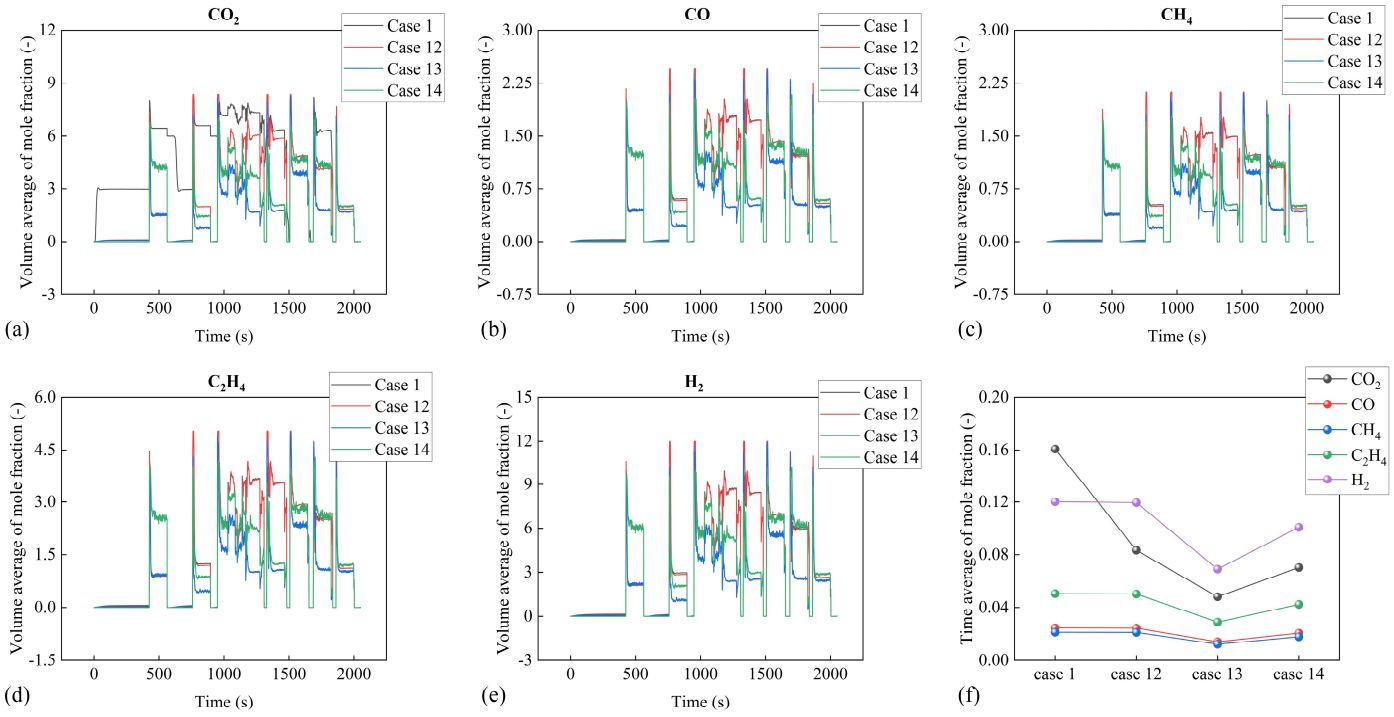

Figure 14. Influence of thermal runaway gas concentration when the battery upside down. (**a**) Volume average of mole fraction of CO_2. (**b**) Volume average of mole fraction of CO. (**c**) Volume average of mole fraction of CH_4. (**d**) Volume average of mole fraction of C_2H_4. (**e**) Volume average of mole fraction of H_2. (**f**) Time average of mole fraction.

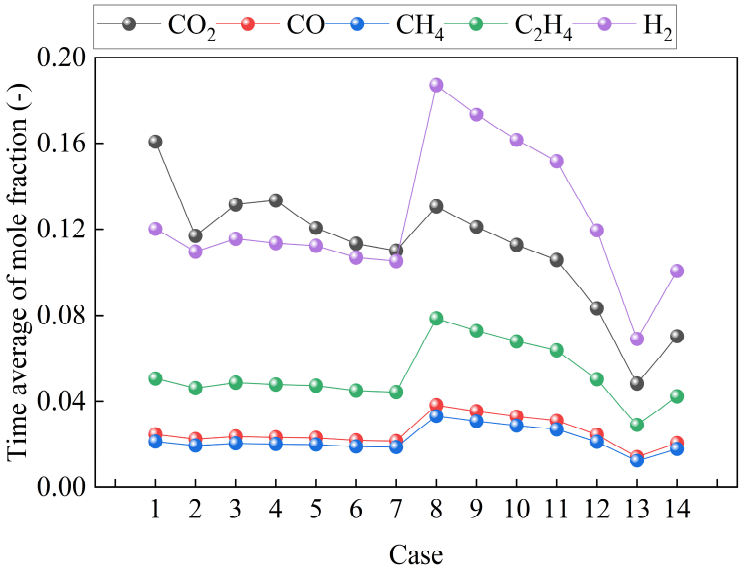

Figure 15. Thermal runaway exhausting method summary.

5. Conclusions

The paper discusses the impact of different flow channel designs on combustible gas accumulation during thermal runaway venting. The research involved ARC experiments and cell module thermal runaway propagation experiments, leading to the development of a thermal runaway resistance network model. Experimental results showed the cell's self-generating heat temperature to be 166.92 °C, with an onset temperature of thermal runaway at 274.00 °C and a maximum temperature of 607 °C. Thermal runaway propagation was calculated using the thermal resistance network model. The accumulation of combustible gas after thermal runaway venting was examined using ANSYS Fluent under various flow channel scenarios.

The study found that air intake from the top of the cell module resulted in better exhaust compared to intake from the side. Increasing the intake mass flow rate improved the exhaust effect. While the average gas concentration of the top intake was lower than that of the side intake, the side intake achieved a more stable gas concentration. The optimal solution involved inverting the cell to allow both sides and the bottom of the module to exhaust simultaneously, leading to a 42.69% reduction in the time average mole fraction compared to exhaust on both sides of the cell.

Author Contributions: Conceptualization, S.Z. and X.Z.; methodology, S.Z.; software, S.Z.; validation, X.Z.; formal analysis, S.Z.; investigation, S.Z.; resources, C.X.; data curation, S.Z.; writing—original draft preparation, S.Z.; writing—review and editing, S.Z.; visualization, S.Z.; supervision, S.Z.; project administration, S.Z.; funding acquisition, C.X., Y.W., J.Q. and X.F.; All authors have read and agreed to the published version of the manuscript.

Funding: This work is supported by the National Key Technologies Research and Development Program Scientific and Technological Strategic Innovation Cooperation (#2022YFE0207900). This work is supported by the Innovative Research Group Project of the National Natural Science Foundation of China [52076121]. National Natural Science Foundation of China (Youth Program Grant No. 52207240) Shandong Province Science and Technology Foundation (Youth Program Grant No. ZR2022QE099) Shandong Province Excellent youth & innovation team Foundation (Grant No. 2023KJ323).

Data Availability Statement: The data that supported the findings of this study are available from the corresponding author upon reasonable request.

Conflicts of Interest: Authors Songtong Zhang, Xiayu Zhu, Jingyi Qiu were employed by Chemical Defense Institute. The remaining authors declare that the research was conducted in the absence of any commercial or financial relationships that could be construed as a potential conflict of interest.

List of Symbols

ρ	Density
C_p	Heat capacity at constant pressure
T	Temperature
Q_{gen}	Heat source item
Q_{con}	Conduction heat transfer
Q_{cov}	Convection heat transfer
Q_{rad}	Radiative heat transfer
V	Volume
c	Energy fraction
λ	Thermal conductivity
A	Area
h	Convective heat transfer coefficient
ε	Surface emissivity
σ	Stefan-Boltzmann constant
S_ε	Turbulent dissipation rate source term
S_h	General scalar source term
S_i	Source term for the ith species
S_k	Turbulent kinetic energy source term
S_m	Mass source term
t	time
$\vec{v}$	Velocity vector
Y_i	Mass fraction of the ith species
Y_M	Turbulence dissipation from fluctuating dilatation
ε	Turbulent dissipation rate
μ	Molecular viscosity
μ_T	Turbulent viscosity
ν	Dynamic viscosity
σ_k	Turbulent Prandtl number for turbulent kinetic energy
σ_ε	Turbulent Prandtl number for turbulent dissipation rate
$\overline{\overline{\tau}}$	Stress tensor
$\overline{\overline{\tau}}_T$	Turbulent stress tensor

References

1. Xu, C.; Fan, Z.; Zhang, M.; Wang, P.; Wang, H.; Jin, C.; Peng, Y.; Jiang, F.; Feng, X.; Ouyang, M. A Comparative Study of the Venting Gas of Lithium-Ion Batteries during Thermal Runaway Triggered by Various Methods. *Cell Rep. Phys. Sci.* **2023**, *4*, 101705. [CrossRef]
2. Li, J.; Wang, P.; Gao, Y.; Guan, D.; Li, S. Quantitative Power Flow Characterization of Energy Harvesting Shock Absorbers by Considering Motion Bifurcation. *Energies* **2022**, *15*, 6887. [CrossRef]
3. Li, J.; Wang, P.; Guan, D.; Gao, Y. Damping Characterization of Electromagnetic Shock Absorbers by Considering Engagement and Disengagement. *Iran. J. Sci. Technol.-Trans. Mech. Eng.* **2022**, *47*, 1215–1264. [CrossRef]
4. Huang, W.; Feng, X.; Han, X.; Zhang, W.; Jiang, F. Questions and Answers Relating to Lithium-Ion Battery Safety Issues. *Cell Rep. Phys. Sci.* **2021**, *2*, 100285. [CrossRef]
5. Xu, J.; Mei, W.; Zhao, C.; Liu, Y.; Zhang, L.; Wang, Q. Study on Thermal Runaway Mechanism of 1000 MAh Lithium Ion Pouch Cell during Nail Penetration. *J. Therm. Anal. Calorim.* **2021**, *144*, 273–284. [CrossRef]
6. Jin, C.; Sun, Y.; Wang, H.; Zheng, Y.; Wang, S.; Rui, X.; Xu, C.; Feng, X.; Wang, H.; Ouyang, M. Heating Power and Heating Energy Effect on the Thermal Runaway Propagation Characteristics of Lithium-Ion Battery Module: Experiments and Modeling. *Appl. Energy* **2022**, *312*, 118760. [CrossRef]
7. Ren, D.; Feng, X.; Lu, L.; He, X.; Ouyang, M. Overcharge Behaviors and Failure Mechanism of Lithium-Ion Batteries under Different Test Conditions. *Appl. Energy* **2019**, *250*, 323–332. [CrossRef]
8. Fernandes, Y.; Bry, A.; de Persis, S. Identification and Quantification of Gases Emitted during Abuse Tests by Overcharge of a Commercial Li-Ion Battery. *J. Power Sources* **2018**, *389*, 106–119. [CrossRef]
9. Wang, Q.; Ping, P.; Zhao, X.; Chu, G.; Sun, J.; Chen, C. Thermal Runaway Caused Fire and Explosion of Lithium Ion Battery. *J. Power Sources* **2012**, *208*, 210–224. [CrossRef]
10. Finegan, D.P.; Darcy, E.; Keyser, M.; Tjaden, B.; Heenan, T.M.M.; Jervis, R.; Bailey, J.J.; Vo, N.T.; Magdysyuk, O.V.; Drakopoulos, M.; et al. Identifying the Cause of Rupture of Li-Ion Batteries during Thermal Runaway. *Adv. Sci.* **2017**, *5*, 1700369. [CrossRef]

11. Liu, P.; Li, Y.; Mao, B.; Chen, M.; Huang, Z.; Wang, Q. Experimental Study on Thermal Runaway and Fire Behaviors of Large Format Lithium Iron Phosphate Battery. *Appl. Therm. Eng.* **2021**, *192*, 116949. [CrossRef]
12. Kim, J.; Mallarapu, A.; Finegan, D.P.; Santhanagopalan, S. Modeling Cell Venting and Gas-Phase Reactions in 18650 Lithium Ion Batteries during Thermal Runaway. *J. Power Sources* **2021**, *489*, 229496. [CrossRef]
13. Zlochower, I.A.; Green, G.M. The Limiting Oxygen Concentration and Flammability Limits of Gases and Gas Mixtures. *J. Loss Prev. Process. Ind.* **2009**, *22*, 499–505. [CrossRef]
14. Li, W.; Rao, S.; Xiao, Y.; Gao, Z.; Chen, Y.; Wang, H.; Ouyang, M. Fire Boundaries of Lithium-Ion Cell Eruption Gases Caused by Thermal Runaway. *iScience* **2021**, *24*, 102401. [CrossRef]
15. Wang, H.; Wang, Q.; Zhao, Z.; Jin, C.; Xu, C.; Huang, W.; Yuan, Z.; Wang, S.; Li, Y.; Zhao, Y.; et al. Thermal Runaway Propagation Behavior of the Cell-to-Pack Battery System. *J. Energy Chem.* **2023**, *84*, 162–172. [CrossRef]
16. Srinivasan, R.; Thomas, M.E.; Airola, M.B.; Carkhuff, B.G.; Frizzell-Makowski, L.J.; Alkandry, H.; Reuster, J.G.; Oguz, H.N.; Green, P.W.; La Favors, J.; et al. Preventing Cell-to-Cell Propagation of Thermal Runaway in Lithium-Ion Batteries. *J. Electrochem. Soc.* **2020**, *167*, 020559. [CrossRef]
17. Jin, C.; Sun, Y.; Yao, J.; Feng, X.; Lai, X.; Shen, K.; Wang, H.; Rui, X.; Xu, C.; Zheng, Y.; et al. No Thermal Runaway Propagation Optimization Design of Battery Arrangement for Cell-to-Chassis Technology. *eTransportation* **2022**, *14*, 100199. [CrossRef]
18. Jin, C.; Sun, Y.; Wang, H.; Lai, X.; Wang, S.; Chen, S.; Rui, X.; Zheng, Y.; Feng, X.; Wang, H.; et al. Model and Experiments to Investigate Thermal Runaway Characterization of Lithium-Ion Batteries Induced by External Heating Method. *J Power Sources* **2021**, *504*, 230065. [CrossRef]
19. Huang, Z.; Yu, Y.; Duan, Q.; Qin, P.; Sun, J.; Wang, Q. Heating Position Effect on Internal Thermal Runaway Propagation in Large-Format Lithium Iron Phosphate Battery. *Appl. Energy* **2022**, *325*, 119778. [CrossRef]
20. Jia, Z.; Song, L.; Mei, W.; Yu, Y.; Meng, X.; Jin, K.; Sun, J.; Wang, Q. The Preload Force Effect on the Thermal Runaway and Venting Behaviors of Large-Format Prismatic LiFePO4 Batteries. *Appl. Energy* **2022**, *327*, 120100. [CrossRef]
21. Zhang, W.; Liang, Z.; Yin, X.; Ling, G. Avoiding Thermal Runaway Propagation of Lithium-Ion Battery Modules by Using Hybrid Phase Change Material and Liquid Cooling. *Appl. Therm. Eng.* **2021**, *184*, 116380. [CrossRef]
22. Song, L.; Huang, Z.; Mei, W.; Jia, Z.; Yu, Y.; Wang, Q.; Jin, K. Thermal Runaway Propagation Behavior and Energy Flow Distribution Analysis of 280 Ah LiFePO4 Battery. *Process Saf. Environ. Prot.* **2023**, *170*, 1066–1078. [CrossRef]
23. Meng, L.; See, K.W.; Wang, G.; Wang, Y.; Zhang, Y.; Zang, C.; Xie, B. Explosion-Proof Lithium-Ion Battery Pack—In-Depth Investigation and Experimental Study on the Design Criteria. *Energy* **2022**, *249*, 123715. [CrossRef]
24. Wang, H.; Xu, H.; Zhang, Z.; Wang, Q.; Jin, C.; Wu, C.; Xu, C.; Hao, J.; Sun, L.; Du, Z.; et al. Fire and Explosion Characteristics of Vent Gas from Lithium-Ion Batteries after Thermal Runaway: A Comparative Study. *eTransportation* **2022**, *13*, 100190. [CrossRef]
25. Wei, G.; Huang, R.; Zhang, G.; Jiang, B.; Zhu, J.; Guo, Y.; Han, G.; Wei, X.; Dai, H. A Comprehensive Insight into the Thermal Runaway Issues in the View of Lithium-Ion Battery Intrinsic Safety Performance and Venting Gas Explosion Hazards. *Appl. Energy* **2023**, *349*, 121651. [CrossRef]
26. Huang, W.; Feng, X.; Pan, Y.; Jin, C.; Sun, J.; Yao, J.; Wang, H.; Xu, C.; Jiang, F.; Ouyang, M. Early Warning of Battery Failure Based on Venting Signal. *J. Energy Storage* **2023**, *59*, 106536. [CrossRef]
27. He, C.X.; Yue, Q.L.; Chen, Q.; Zhao, T.S. Modeling Thermal Runaway of Lithium-Ion Batteries with a Venting Process. *Appl. Energy* **2022**, *327*, 120110. [CrossRef]
28. Cai, T.; Valecha, P.; Tran, V.; Engle, B.; Stefanopoulou, A.; Siegel, J. Detection of Li-Ion Battery Failure and Venting with Carbon Dioxide Sensors. *eTransportation* **2021**, *7*, 100100. [CrossRef]
29. Coman, P.T.; Mátéfi-Tempfli, S.; Veje, C.T.; White, R.E. Modeling Vaporization, Gas Generation and Venting in Li-Ion Battery Cells with a Dimethyl Carbonate Electrolyte. *J. Electrochem. Soc.* **2017**, *164*, A1858–A1865. [CrossRef]
30. Kong, D.; Wang, G.; Ping, P.; Wen, J. A Coupled Conjugate Heat Transfer and CFD Model for the Thermal Runaway Evolution and Jet Fire of 18650 Lithium-Ion Battery under Thermal Abuse. *eTransportation* **2022**, *12*, 100157. [CrossRef]
31. Feng, X.; Lu, L.; Ouyang, M.; Li, J.; He, X. A 3D Thermal Runaway Propagation Model for a Large Format Lithium Ion Battery Module. *Energy* **2016**, *115*, 194–208. [CrossRef]
32. Zhang, F.; Wang, P.; Yi, M. Design Optimization of Forced Air-Cooled Lithium-Ion Battery Module Based on Multi-Vents. *J. Energy Storage* **2021**, *40*, 102781. [CrossRef]